

RAANet: Range-Aware Attention Network for LiDAR-based 3D Object Detection with Auxiliary Density Level Estimation

Yantao Lu^{1*}, Xuetao Hao^{2*}, Shiqi Sun³, Weiheng Chai¹, Yu Ding⁴, Muchenxuan Tong², and Senem Velipasalar¹

¹ Syracuse University {ylu25, wchai01, svelipas}@syr.edu

² Didi Labs {xuetaohao, tongmuchenxuan}@didiglobal.com

³ Duke University shiqi.sun@duke.edu

⁴ Baidu Security yuding@baidu.com

Abstract. Among the 3D object detection methodologies for autonomous driving, encoding point clouds into a bird’s eye view (BEV) has been demonstrated to be both effective and efficient. Different from perspective views, farther objects of the same type do not appear smaller in the BEV, they contain sparser point cloud features. This fact weakens BEV feature extraction using shared-weight convolutional layers. In order to address this challenge, we propose Range-Aware Attention Network (RAANet), which extracts BEV feature maps with rich spatial and distance information. Moreover, a novel auxiliary loss is proposed for density estimation to further enhance the detection accuracy of RAANet for occluded objects. Our proposed RAA convolution is compatible to be integrated into any CNN architecture used for the BEV detection. Experiments on nuScenes dataset demonstrate that our proposed approach outperforms the state-of-the-art methods for LiDAR-based 3D object detection, with real-time of 16 Hz.

Keywords: 3D Object Detection, Autonomous Driving, Point Clouds, Bird’s Eye View, Attention Convolution

1 Introduction

With rapid improvement of processing units, and thanks to the extraordinary success of deep neural networks, the perception of autonomous driving has been flourishing in recent years. 3D object detection from LiDAR sensors is one of the important capabilities for autonomous driving. Early works employ 3D convolutional neural networks, which have slow processing speeds and large memory requirements. In order to decrease the memory requirements and provide real-time processing, recent methodologies leverage voxelization and bird’s eye view (BEV) projection. Voxelization is widely implemented as a preprocessing method for 3D point clouds because of the computing efficiency, provided by more structured data, and performance accuracy [10][29][28][20][21]. In general, voxelization divides a point cloud into an evenly spaced grid of voxels, and then

* Equal contribution

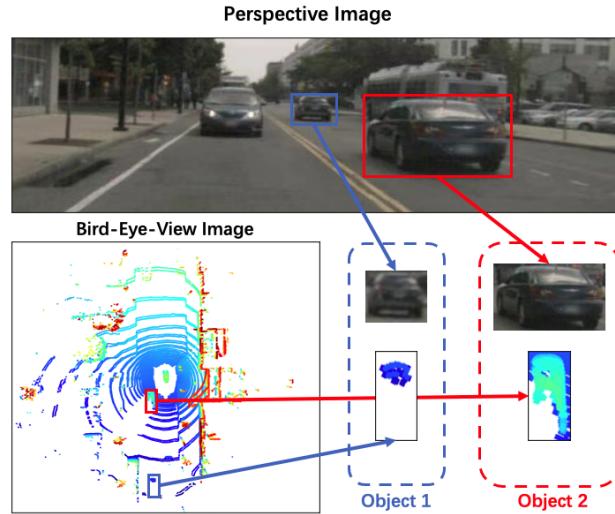


Fig. 1: **Motivation.** Different from camera images with perspective distortion, in BEV, objects that are farther from the ego-vehicle do not appear in smaller sizes, but contain sparser set of LiDAR points. Thus, an object in BEV may appear different depending on the distance to ego-vehicle, which weakens BEV feature extraction using shared-weight CNNs.

assigns 3D LiDAR points to their respective voxels. The output space preserves the Euclidean distance between objects and avoids overlapping of bounding boxes. This fact keeps object size variation in a relatively small range, regardless of their distance from the LiDAR, which benefits the shape regression during training. However, as shown in Figure 1, the voxels that are farther away from the ego-vehicle contain significantly fewer LiDAR points than the near ones. This leads to a situation where different representations may be extracted for an object at different distances to the ego-vehicle. In contrast to perspective view, where feature elements are location-agnostic, BEV feature maps are location sensitive. Thus, different convolutional kernel weights should be applied to different locations of the feature map. In other words, location information should be introduced to the feature maps, and the convolutional kernels should be adjustable to the location information of corresponding feature maps.

In this paper, we propose Range-Aware Attention Network (RAANet), which contains novel Range-Aware Attention Convolutional layer (RAAConv) designed for object detection from LiDAR BEV. RAAConv is composed of two independent convolutional branches and attention maps, which is sensitive to the location information of the input feature map. Our approach is inspired by properties of BEV images, which are illustrated in Fig. 1. Points get more sparse as the distance between an objects and ego-vehicle increases. Ideally, for BEV feature maps, elements at different locations should be processed by different convolution kernels. However, applying different kernels will significantly increase the computational expense. In order to utilize the location information during BEV feature extraction, while avoiding heavy computation, we regard a BEV feature map as a composition of sparse features and dense features. We apply

two different convolution kernels to simultaneously extract sparse and dense features. Each extracted feature map has half the channel size of the final output. Meanwhile, range and position encodings are generated based on the input shape. Then, each range-aware attention heatmap is computed from the corresponding feature map and the range and position encodings. Finally, the attention heatmaps are applied on the feature maps to enhance feature representation. The feature maps generated from two branches are concatenated channel-wisely as the RAACnv output. Details are presented in Sec. 3.2.

In addition, the side effect from occlusion cannot be ignored, since the same object may have different point distributions under different amounts of occlusion. Thus, we propose an efficient auxiliary branch, referred to the Auxiliary Density Level Estimation Module (ADLE), allowing RAANet to take occlusion into consideration. Since annotating various occlusions is a time consuming and expensive task, we design the ADLE to estimate a density level for each object. If there is no occlusion, the point density levels for near objects are higher than those of far objects. However, if a near object is occluded, its point density level decreases. Therefore, by combining range information and density level information, we are able to simulate the occlusion information. ADLE is only used in the training stage for providing density information guidance, and can be removed in inference state for computational efficiency.

Contributions. The main contributions of this work include the following:

- We propose the RAACnv layer, which allows LiDAR-based detectors to extract more representative BEV features. In addition, RAACnv layer can be integrated into any CNN architecture used for LiDAR BEV.
- We propose a novel auxiliary loss for density estimation to help the main network learn occlusion related features. This proposed density level estimator further enhances the detection accuracy of RAANet on occluded objects as well.
- We propose the Range-Aware Attention Network (RAANet), which integrates the aforementioned RAA and ADLE modules. RAANet is further optimized by generating anisotropic Gaussian heatmap based on the ground truth, which is introduced in Sec. 3.4.
- The code is available at an anonymous GitHub repo. [1].

2 Related Work

In recent years, many methods have been presented in the field of 3D object detection. Pixor [23] performs the voxelization via a customized encoding algorithm of the point clouds. However, the hand-craft design of voxelization limits the generalization and adaptation of Pixor. Hence, to overcome this shortcoming, VoxelNet [29] proposes a PointNet and 3D convolutional layer to voxelize the points clouds autonomously. Compared to VoxelNet, SECOND [22] improves the inference time with the sparsely embedded convolutional layers. Although VoxelNet-based methodologies provide powerful encoding schemes of point clouds, researchers are still exploring new effective methods. In particular, PointPillar [10] discards 3D convolutional layers and voxelization, and presents a new encoding scheme called pillar. They merge the points of z-axis and then project them into BEV space. Therefore, the points could be processed by 2D convolutions. They propose an end-to-end pipeline with only 2D convolutional layers based on pillars, which significantly improves the processing speed.

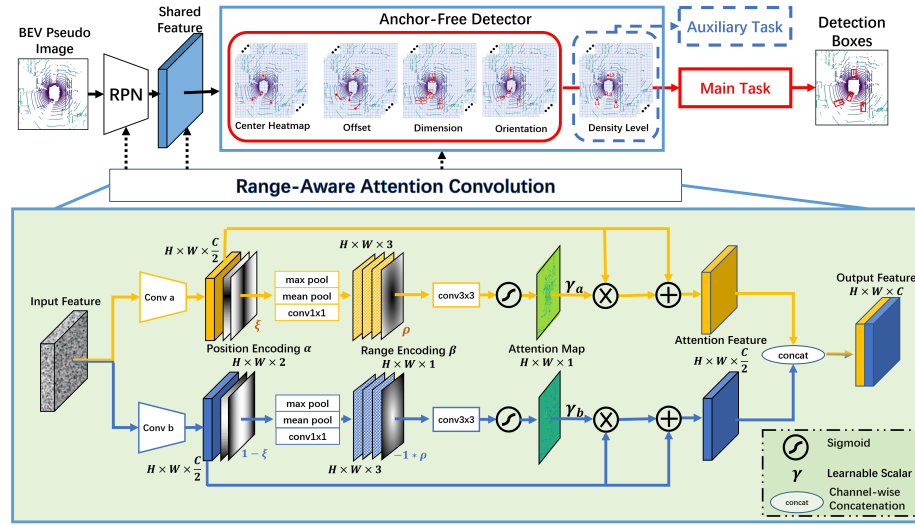


Fig. 2: **Overview of the proposed network.** The RPN is designed to extract the shared feature from a BEV pseudo image. Then, the main detection heads and an auxiliary density estimation head are appended. The auxiliary head only exists during training and is omitted during inference. Finally, 3D bounding boxes are obtained from the main task. Our proposed RAACONV layer, illustrated in the lower part of the figure, replaces the original Conv2D layer. In general, this layer contains two branches, and each branch applies position and range encodings to generate its range-aware attention heatmap. Then, extracted features in each branch are enhanced by the heatmap with a residual architecture. Those enhanced features are concatenated for the final output features.

The aforementioned studies have provided effective and fast methodologies to encode point clouds. However, how to effectively process these encodings and perform precise bounding box regression still remains to be explored further. CenterPoint [25] provides a regression method by focusing on the center points of all bounding boxes, and hence reduces the complexity of rotation. Although the rotation invariance of the center point makes this method accurate and fast, significant amount of positional information is lost because of the top-view encoding and the isotropic Gaussian mask. To avoid these drawbacks, a series of works consider the positional information in the feature extractor. Particularly, CBAM [19] adds spatial attention and channel attention modules into the convolutional layers. Although this scheme provides a new insight of adding attention mechanism, it still cannot well encode the complicated spatial information from the LiDAR point clouds. Thus, it is necessary to design a novel convolutional network to utilize the location and density information from the point clouds.

3 Range-Aware Attention Network

3.1 Overview of RAANet

The main architecture of our proposed Range-Aware Attention Network (RAANet) is presented in Fig. 2. We incorporate ideas from CenterNet [27][25] to build an anchor-free detector, and also introduce two novel modules: the Range-Aware Attention Convolutional Layer (RAAConv) and the Auxiliary Density Level Estimation Module (ADLE).

RAANet takes the 3D LiDAR points as input and generates a set of 3D oriented bounding boxes as the output. Inspired by VoxelNet [29], we implement a feature extractor with 3D sparse convolutional network to extract the BEV feature map from voxelized point clouds. This resulting feature map is reshaped and formed into a BEV pseudo image, which can be regarded as a multi-channel 2D image. The Region Proposal Network (RPN) takes this BEV pseudo image as input and employs multiple down-sample and up-sample blocks to generate a high-dimensional feature map. In addition to the detection heads in main task, we propose an auxiliary task for density level estimation to achieve better detection performance. Meanwhile, the RAAConv layers are utilized in all convolutional modules shown as Fig. 2. Center probability heatmap is generated from the detector head, and maximums in local neighborhoods are treated as the centers of ground-truth bounding boxes (bbox). The regression of bbox attributes, including offsets, dimensions and orientations, are computed from the other heads in the main detection task. Parallel to the main task, the proposed ADLE, as an auxiliary task, estimates density level for each bounding box. In general, ADLE classifies each bounding box into different density levels, based on the number of points in each bbox. ADLE is a portable block for the whole network, i.e. it is employed only in the training process and is not used during inference for higher computational efficiency.

For the training phase, we denote the loss components as the heatmap classification loss, bbox regression loss and density-level auxiliary loss as l_{hm} , l_{bbox} and l_{aux} , respectively. The total loss function of RAANet is formulated as

$$l = l_{hm} + \lambda_{bbox} l_{bbox} + \lambda_{aux} l_{aux}, \quad (1)$$

where λ_{bbox} and λ_{aux} are scalar weights for balancing multi-task loss. l_{hm} and l_{aux} are designed as the penalty-reduced focal losses [11][27], and l_{bbox} is designed as the smooth L1 loss.

3.2 Range-Aware Attention Convolutional Layer

We propose the Range-Aware Attention Convolutional Layer (RAAConv), which, by leveraging the specially designed attention blocks, becomes sensitive to range and position information. This is the major difference between the proposed RAAConv and traditional convolutional layer. RAAConv is employed in the aforementioned RPN and detection heads. As shown in Fig. 2, RAAConv first utilizes two sets of convolutional kernels to extract an intermediate feature map for each branch. Then, the position encodings are generated and embedded into intermediate feature maps. Two range-aware heatmaps are calculated by a series of convolution and pooling operations using the intermediate feature maps and range encodings. More specifically, given

an input feature map $I \in \mathbb{R}^{H_{in} \times W_{in} \times C_{in}}$, two separate intermediate feature maps, $\mathbf{F}_a, \mathbf{F}_b \in \mathbb{R}^{H_{out} \times W_{out} \times \frac{C_{out}}{2}}$, are generated by

$$\mathbf{F}_i = \zeta(\mathbf{I}, w_{\mathbf{F}}^i), i \in a, b, \quad (2)$$

where $\zeta(\cdot)$ represents convolution operation and $w_{\mathbf{F}}^i$ denotes the corresponding convolution kernel.

Meanwhile, the position encoding map $\xi \in \mathbb{R}^{H_{out} \times W_{out} \times 2}$ and range encoding map $\rho \in \mathbb{R}^{H_{out} \times W_{out} \times 1}$ are generated from the intermediate feature map \mathbf{F}_a . ξ and ρ are calculated from shape information and do not depend on the values inside the tensor F_a . There are two components of ξ : row encoding r and column encoding c . ξ and ρ are generated as follows:

$$\begin{aligned} r_{ij} &= \frac{2|i - \frac{H}{2}|}{H}, \quad c_{ij} = \frac{2|j - \frac{W}{2}|}{W} \\ \rho_{ij} &= 2\sqrt{r_{ij}^2 + c_{ij}^2} - 1 \\ s.t. \quad &i \in \{1, 2, \dots, H\}, \quad j \in \{1, 2, \dots, W\} \end{aligned} \quad (3)$$

Values of r, c are bounded in $[0, 1]$. Values of ρ are bounded in $[-1, 1]$.

Since the proposed network is designed by using two convolution kernels to extract dense and sparse features separately, we append ξ to intermediate feature map \mathbf{F}_a channel-wise, and reversely append $1 - \xi$ to \mathbf{F}_b . The generated features are denoted as \mathbf{F}'_a and \mathbf{F}'_b . Maximum pooling, mean pooling and 1×1 conv2D are applied on \mathbf{F}'_a and \mathbf{F}'_b separately to obtain the spatial embeddings \mathbf{F}_a^ξ and \mathbf{F}_b^ξ . Then, similar to positional appending, the range encoding map ρ is appended to \mathbf{F}_a^ξ , and $-\rho$ is appended to \mathbf{F}_b^ξ . The appended features are processed by a 3×3 conv2D layer followed by sigmoid activation to obtain the range-aware attention heatmaps \mathbf{f}_a and \mathbf{f}_b . The heatmaps \mathbf{f}_a and \mathbf{f}_b are then multiplied by learnable scalars γ_a and γ_b separately. γ_a and γ_b are initialized as 1.0 and gradually learn the weights during training [26]. The output feature maps \mathbf{F}''_a and \mathbf{F}''_b are calculated from $\mathbf{F}'_a, \mathbf{f}_a, \gamma_a$, and $\mathbf{F}'_b, \mathbf{f}_b, \gamma_b$ using a residual connection, which is defined as:

$$\mathbf{F}''_i = (\gamma_i \mathbf{f}_i) \otimes \mathbf{F}'_i + \mathbf{F}'_i, \quad i \in a, b \quad (4)$$

where \otimes is the operation performing channel-wise stacking and element-wise multiplication. The final output for RAAConv is the channel-wise concatenation of \mathbf{F}''_a and \mathbf{F}''_b , which has size of $H_{out} \times W_{out} \times C_{out}$.

It is worth noting that the proposed RAAConv can be readily plugged in any convolutional network for LiDAR BEV detection.

3.3 Auxiliary Density Level Estimation Module (ADLE)

The Auxiliary Density Level Estimation Module (ADLE) is an additional classification head that is parallel to the main task heads. The ADLE indicates density level for each bbox. In general, we design ADLE to estimate the relative number of LiDAR points inside a detected bbox. We have empirically found that this estimation is straightforward yet helpful to the detector. Moreover, we divide the number of points into three density bins and let ADLE perform a classification task, instead of a value regression

task, which helps training converge better. More specifically, the three bins are labeled as sparse (label 1), adequate (label 2) and dense (label 3). We have statistically analyzed the distribution of the number of points and employed two thresholds T_0^i, T_1^i to determine the density level for each object class i . The three density levels are defined as: where n denotes the number of points, and D_i represents the density level for the i -th class. As shown in Fig. 3, the unoccluded instances near the ego-vehicle have high point density levels and faraway instances have low density levels. However, when an instance is occluded, the density level will be lower than the unoccluded case at the same distance. Since we incorporate position and range information into RAAConv, ADLE is able to further help RAAConv extract occlusion information by supervising the point density levels.

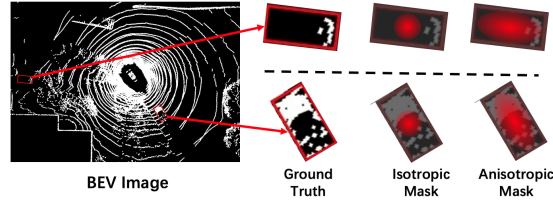


Fig. 3: **Illustration of Anisotropic Gaussian Mask.** Traditional Isotropic Gaussian Mask neglects the rotation of the bounding box. We propose an Anisotropic Gaussian Mask to better fit for the ground truth. *The Anisotropic mask is able to introduce the heading information, which is beneficial to bbox regression as well.*

3.4 Anisotropic Gaussian Mask

Anisotropic Gaussian Mask represents the centerness probability for each position in a annotated bbox. The centerness heatmap is generated as the ground truth for the classification head. In this work, we propose an Anisotropic Gaussian Mask, shown in Fig. 3, as the method of 2D Gaussian distribution generation, to be used for the centerness probabilities of a given oriented bbox. More specifically, the Gaussian distribution $N(\mu, \Sigma)$ is designed in anisotropic way: the σ values for the 2 dimensions, denoted as σ_0, σ_1 , which are the diagonals of Σ , are different, and their values are determined from the length and width of the bbox, respectively. The procedure of generating the center heatmap, denoted by \mathfrak{M} , can be formulated as:

$$\mathfrak{M}_{C_H, C_W, H, W, s}(x, y) = \mathbb{1}_{\mathfrak{B}}(N_{\mu, \Sigma}(x, y)) \quad (5)$$

where,

$$\begin{aligned} \mathfrak{B} &= \{x \in [C_W - \frac{W}{2}, C_W + \frac{W}{2}] \cap y \in [C_H - \frac{H}{2}, C_H + \frac{H}{2}]\} \\ \mu &= [C_W, C_H]^T \\ \Sigma &= \begin{bmatrix} W/d_{cls} & 0 \\ 0 & H/d_{cls} \end{bmatrix} \end{aligned} \quad (6)$$

and (C_H, C_W) and (H, W) denote the center location and dimensions of a bbox, respectively. s indicates the ground truth class for the bbox. $\mathbb{1}(\cdot)$ is the indicator function and \mathfrak{B} denotes the set of locations that are inside the bbox. d_{cls} is a decay factor that decides the sharpness of generated heatmap. The value of d_{cls} depends on the class of the given bbox.

3.5 Loss Functions

Following Eq. (1), the center heatmap loss L_{hm} is defined as:

$$L_{hm} = -\frac{1}{N} \sum_{\tilde{p}} \{(1-h)^\alpha \log(h) I_{\hat{h} > 1-\epsilon} + (1-\hat{h})^\beta h^\alpha \log(1-h) I_{\hat{h} \leq 1-\epsilon}\}, \quad (7)$$

where h and \hat{h} are the predicted and ground-truth heatmap values, respectively. ϵ is a small value for numerical stability. α and β are the parameters to control penalty-reduced focal loss. For all the experiments, we follow the setting in [17]: $\epsilon = 1e-3$, $\alpha = 2$ and $\beta = 4$.

The bounding box head is responsible for location, dimension and orientation regression, which are represented by the following parameters: $\Gamma = [\delta_x, \delta_y, \delta_z, l, w, h, \theta]$, where $\delta_x, \delta_y, \delta_z$ are the box center offsets with respect to the corresponding voxel centers; and l, w, h and θ denote the length, width, height and yaw of a bounding box. We apply smoothed L1 (SL1) losses to regress $\sin(\theta)$ and $\cos(\theta)$ for the θ attribute, and directly regress actual values for other attributes:

$$L_{\theta_i} = SL1(\sin(\theta_i) - \sin(\hat{\theta}_i)) + SL1(\cos(\theta_i) - \cos(\hat{\theta}_i)) \quad (8)$$

$$L_{\Gamma_i \setminus \theta} = SL1(\Gamma_i \setminus \theta - \hat{\Gamma}_i \setminus \hat{\theta}) \quad (9)$$

where, $\hat{\cdot}$ denotes ground truth values corresponding to original symbols. The total loss for box regression is:

$$L_{box} = \frac{\mathbb{1}_i}{N} \sum_i (L_{\theta_i} + L_{\Gamma_i \setminus \theta}), \quad (10)$$

where N is the number of box samples and $\mathbb{1}_i$ equals 1 if the ground truth heatmap value of the i th feature map pixel is larger than a threshold τ , which is set to 0.2 in the experiments.

4 Experiments

We introduce the implementation details of the RAANet and evaluate its performance in multiple experiments. The inference results are uploaded to and evaluated by the nuScenes official benchmark [12]. The diagnostic analysis of each component is shown in the ablation studies.

	Car	Truck	Bus	Trailer	Cons. Veh.	Ped.	M.cyc.	Bicycle	Traffic Cone	Barrier	mAP
PointPillars [10]	0.760	0.310	0.321	0.366	0.113	0.640	0.342	0.140	0.456	0.564	0.401
SA-Det3D [2]	0.812	0.438	0.572	0.478	0.113	0.733	0.321	0.079	0.606	0.553	0.470
InfoFocus [18]	0.779	0.314	0.448	0.373	0.107	0.634	0.290	0.061	0.465	0.478	0.395
CyliNetRG [14]	0.850	0.502	0.569	0.526	0.191	0.843	0.586	0.298	0.791	0.690	0.585
SARPNET [24]	0.599	0.187	0.194	0.180	0.116	0.694	0.298	0.142	0.446	0.383	0.324
PanoNet3D [7]	0.801	0.454	0.540	0.517	0.151	0.791	0.531	0.313	0.719	0.629	0.545
PolarStream [6]	0.809	0.381	0.471	0.414	0.195	0.802	0.614	0.299	0.753	0.640	0.538
MEGVII [30]	0.811	0.485	0.549	0.429	0.105	0.801	0.515	0.223	0.709	0.657	0.528
PointRCNN[15]	0.810	0.472	0.563	0.510	0.141	0.766	0.422	0.134	0.667	0.614	0.510
SSN-v2 [31]	0.824	0.418	0.461	0.480	0.175	0.756	0.489	0.246	0.601	0.612	0.506
HotSpotNet [5]	0.831	0.509	0.564	0.533	0.230	0.813	0.635	0.366	0.730	0.716	0.593
MMDec3D [8]	0.847	0.490	0.541	0.528	0.216	0.793	0.560	0.387	0.714	0.674	0.575
CenterPoint [25]	0.852	0.535	0.636	0.560	0.200	0.846	0.595	0.307	0.784	0.711	0.603
CVCNet-ens [4]	0.826	0.495	0.594	0.511	0.162	0.830	0.618	0.388	0.697	0.697	0.582
Our RAANet-lite	0.858	0.543	0.634	0.552	0.235	0.855	0.620	0.319	0.789	0.740	0.615
Our RAANet	0.860	0.546	0.636	0.553	0.237	0.856	0.633	0.340	0.794	0.749	0.620

Table 1: **Comparison with the state-of-the-art models** for 3D detection on the nuScenes test dataset. We show AP scores for each class and overall mAP scores. The best results are marked in **bold** and second best results are marked in **blue** color. The RAANet refers to the network that applies RAACnv layers throughout all modules. The RAANet-lite refers to the network that applies RAACnv layers on the detection heads.

4.1 NuScenes Dataset

We primarily perform the evaluation on the nuScenes dataset [3], which is a public, large-scale and challenging dataset for autonomous driving developed by the team at nuTonomy. The full dataset includes approximately 390k LiDAR sweeps and 1.4M object bounding boxes in 40k key frames. The dataset contains 1000 scenes in total and is splitted as 700 for training, 150 for validation and 150 for testing. There are a total of 10 classes: {car, truck, bus, trailer, construction vehicle, traffic cone, barrier, motorcycle, bicycle, pedestrian}. The scenes of 20 sec. length are manually selected to show a diverse and interesting set of driving maneuvers, traffic situations and unexpected behaviors. The dataset was captured with a 32-channel spinning LiDAR sensor with 360 degree horizontal and -30 to +10 degree vertical FOV. The sensor captures points, which are within 70 meters with ± 2 cm accuracy and returns up to 1.39M points per second.

4.2 Implementation Details

RAANet is implemented in PyTorch framework [13] with anchor-free object detection architecture. For the baseline, we use CenterPoint[25] with Isotropic Gaussian Mask and original convolutions. All classes are trained together in a single end-to-end network. The weights λ_{box} and λ_{aux} in loss function (Eq. 1) are set to 0.25 and 0.2 respectively. The resolution for voxelization is set to [0.075m, 0.075m, 0.2m] and the voxelization region is $[-54m, 54m] \times [-54m, 54m] \times [-5m, 3m]$. The decay factor d in Sec. 3.4

is set to 3.0 for large size classes (car, truck, bus, trailer, construction_vehicle), to 6.0 for small object classes (traffic_cone, barrier, motorcycle, bicycle, pedestrian). As for the parameters in Sec. 3.5, we set ϵ , α , β and τ to 0.001, 2.0, 4.0 and 0.2, respectively. More details are provided in the configuration file of our anonymous github repository [1]. Two versions of the RAANet are designed in this work: (i) the full version RAANet applies RAACnv layers throughout all modules; (ii) RAANet-lite version applies RAACnv layers only on the detection heads. Both designs outperform SOTAs. Compared to RAANet, RAANet-lite has faster inference speed, with a small drop on mAP performance.

4.3 Training and Inference

RAANet is trained end-to-end from scratch on $4 \times$ NVIDIA RTX-6000 GPUs. ADAM optimizer [9] with $\beta_1 = 0.9$, $\beta_2 = 0.99$ and One-Cycle learning rate scheduler [16] with maximum $lr = 0.001$ are used during the training. 20 epochs are trained in total and the batch size for each GPU is set to 4. Random flipping along the x -axis and global rotation around the z -axis, with a random angle sampled from $[-\pi/4, \pi/4]$, are implemented as the augmentation strategies in the training process.

During inference, we reuse the checkpoint with the best mean average precision (mAP) value and evaluate on the official nuScenes evaluation detection metric. The detection score threshold is set to 0.1 and IoU threshold is set to 0.2 for non-maximal suppression. The inference latency for full version of RAANet and RAANet-lite are 62 ms and 45 ms per frame, respectively. Both versions satisfy the real-time 3D detection criteria.

4.4 Results

We present the results, obtained on the test set with both our lite-version and full-version models in Table 1. The architecture of the full version model is illustrated in Fig. 2. All detection results are evaluated by average precision (AP) for 3D object detection. Besides CenterPoint, we compare our work with other state-of-the-art models that have either published papers or open-source code. As can be seen in Table 1, RAANet outperforms all the other models in mAP, and RAANet-lite takes the second place. For individual classes, RAANet achieves the best AP for 7 out of 10 classes, and takes the second place for one of the remaining 3 classes. Although trailer and bicycle do not achieve the top performances, they still look comparable to other methods.

4.5 Ablation Studies

In this section, we provide results of the ablation studies for components and critical parameters, which are attention module, decay factor d (for the anisotropic Gaussian mask) and λ_{aux} (weight for the density level estimation loss). The models are evaluated on nuScenes validation set. For computational efficiency, we perform all experiments in this section on 'Car' and 'Pedestrian' classes to represent large and small objects, respectively.

Model	RAAConv			2D Gaussian	ADLE $\lambda_{aux} = 0.25$	AP (%)	
	Dual Branch	Attention	γ			Car	Pedestrian
Baseline	-	-	-	-	-	85.23	84.62
+ RAAConv	✓	✗	✗	✗	✗	85.30	84.71
	✗	✓	✗	✗	✗	85.40	84.95
	✓	✓	✗	✗	✗	85.51	85.30
	✓	✓	✓	✗	✗	85.64	85.41
+ 2D Gaussian	✓	✓	✓	✓	✗	85.90	-
+ auxiliary loss	✓	✓	✓	✓	✓	86.14	85.64

Table 2: **Ablation study of Range-Aware Attention Network.** Various models are built by different combination of three attributes: RAAConv, Anisotropic Gaussian Mask (2D Gaussian for short) and ADLE. For RAAConv, there are four sub-components: dual branch structure, range-aware attention heatmap and learnable scalar γ (Fig. 2). Anisotropic Gaussian Mask is not applied on pedestrian class, since the labeled bboxes have similar widths and lengths.

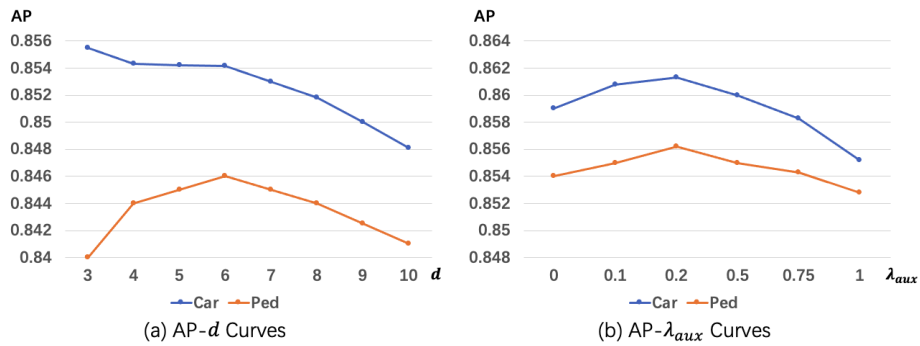


Fig. 4: **Ablation Studies on Anisotropic Gaussian Mask and ADLE.** (a) shows AP results with different Gaussian Σ decay factors, which is denoted as d in Eq. (6). (b) shows different ADLE loss weights denoted as λ_{aux} in Eq. (1). Experiments are based on the baseline model.

Anisotropic Gaussian Mask. We evaluate the performance of Anisotropic Gaussian Mask by varying the decay factor d . The ablation studies in Fig. 4(a) show that Car AP performance has more obvious improvement than the Pedestrian with anisotropic Gaussian mask. One of the probable reasons is that the annotated bboxes for pedestrian class have the similar widths and lengths. This leads the anisotropic Gaussian mask to fall back to the original isotropic Gaussian mask. Additionally, we set $d = 3$ and $d = 6$ for large and the other small objects in main experiments. In general, IOU-based evaluation is more sensitive to small objects than large objects, sharper Gaussian masks help small objects achieve higher accuracies.

Auxiliary Density Level Estimation Module. The AP results obtained with various weights of the loss (λ_{aux}), for the auxiliary component, are shown in Fig. 4(b). The loss weight values are chosen between 0.0 to 1.0. We set $\lambda_{aux} = 0.2$ for the auxiliary loss.

Range-Aware Attention Convolution. Table 2 shows the performance of the baseline as well as several types of the Range-Aware Attention Network. For RAAConv,

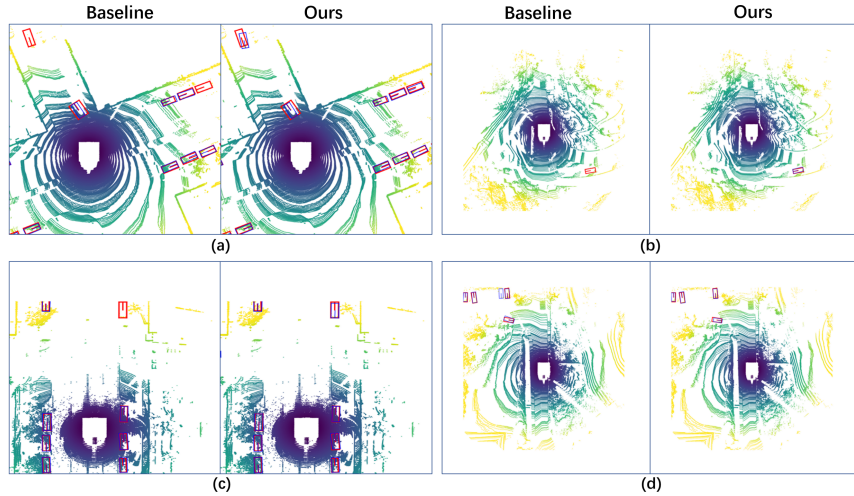


Fig. 5: **Qualitative results.** (Please zoom-in for details). For each image pair, images on the left are the results inferred from the baseline, and the images on the right are the results from the proposed RAANet. Red and blue boxes denote the ground truth and predictions, respectively.

there are three sub-components: dual branch structure, range-aware attention heatmap and learnable scalar γ (Fig. 2). The combination of those three sub-components can generate the optimal gain for the RAACnv. Each aforementioned component contributes to the improvement of detection performance. We observe that the combination of dual-branch structure and range-aware attention achieves up to 0.8% gain on the small object. With learnable scalar γ , the dual-branch attentions can be adaptive to the variation of the training data.

4.6 Generalizability

The proposed RAANet is further evaluated by a different backbone from PointPillar. More specifically, we replace the original 3D voxel-based backbone with 2D pillar-based backbone. The pillar size is set to $(0.2, 0.2)$, which follows [10]. The perception range is set to $[-51.2, 51.2] \times [-51.2, 51.2] \times [-5, 3]$. The baseline is trained with CenterPoint-PointPillar version. As shown in Table 3, our proposed RAANet still generates competitive performance.

4.7 Qualitative Analysis

Pairs of example outputs, obtained by the baseline and the proposed RAANet are provided in Fig. 5 for qualitative comparison. The sample data is selected from nuScenes validation dataset. In a pair, images on the left are the results inferred from the baseline, and the images on the right are the results from the proposed RAANet. It can be observed that RAANet increases true positives and suppresses false positives at the far and occluded regions.

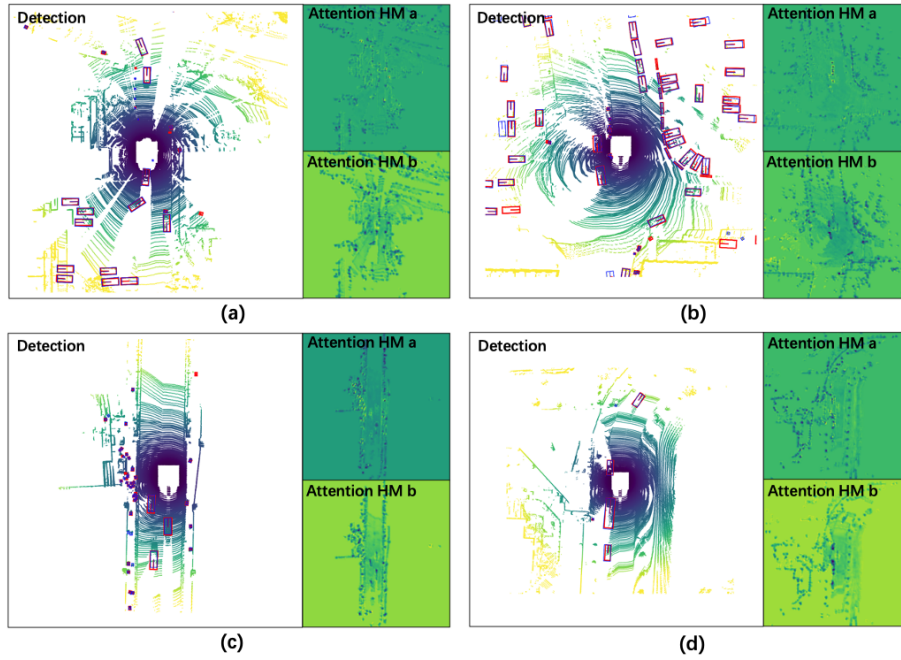


Fig. 6: **Detection and Attention Visualization.** For each sub-figure, the image on the left is the all-class detection result, inferred from our proposed RAANet on the nuScenes validation dataset, and the two images on the right are the attention heatmaps from two convolutional branches in the RAAConv layer. Different color distributions represent how much attentions is paid on the different ranges.

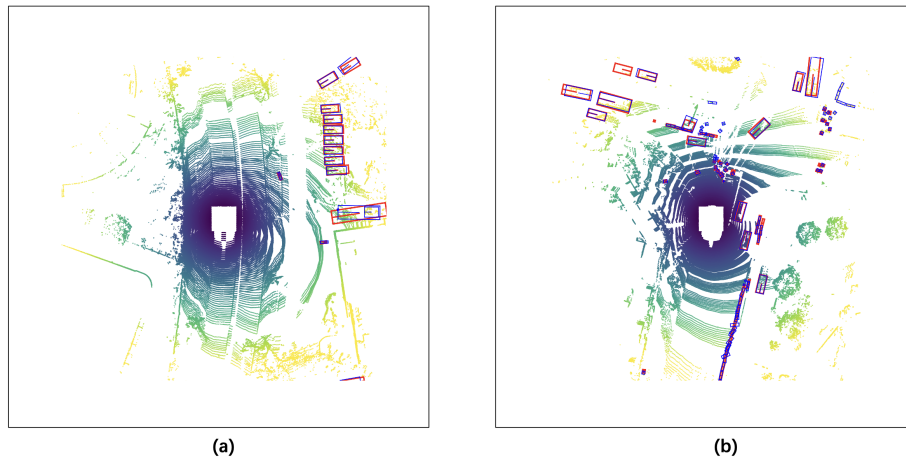


Fig. 7: **Failure Cases.** (a) The far and large objects could cause inaccurate bounding box regression; (b) False positives may appear at the region of sparse point clouds.

Models	RAAConv	2D Gaussian	ADLE	AP(%)	
				Car	Pedestrian
Baseline	✗	✗	✗	83.98	82.80
RAANet	✗	✓	✗	84.32	82.82
	✓	✗	✗	84.43	83.61
	✓	✓	✗	84.69	-
	✓	✓	✓	84.80	83.79

Table 3: **AP results for RAANet with PointPillar Backbone.** The baseline and comparison models are built with PointPillar proposed backbone. Comparison models are composed by various combinations of RAAConv, 2D Gaussian Mask and ADLE.

Fig. 6 shows more visualization examples on all-class detection of the RAANet as well as the attention heatmaps generated from RAAConv. For each sub-figure, the image on the left is the all-class detection result inferred from our proposed RAANet, and the two images on the right are the attention maps from both convolutional branches in the RAAConv layer. It can be observed that both attention modules represent the positional heatmaps based on the Bird’s Eye View. In general, the attention heatmap, from the branch a, highlights the regions with dense point clouds or the ego-vehicle vicinity. The attention heatmap, from the branch b, pays attention to the regions with sparse point clouds or farther distances from ego vehicle. The combination of both branches effectively extracts the powerful BEV features and generates superior 3D object detections.

Fig. 7 shows that some hard examples are misjudged by our proposed method. In (a), although our RAANet successfully generates the detection results for all ground truths, some of the detection headings are not regressed accurately enough due to the long distance and sparse points inside the objects. In (b), some false positives appear on severely occluded regions.

5 Conclusion

In this paper, we have introduced the Range-Aware Attention Network (RAANet) to improve the performance of 3D object detection from LiDAR point clouds. The motivation behind the RAANet is that, in Bird’s Eye View (BEV) LiDAR images, objects appear very different at various distances to the ego-vehicle, and thus, there is a need to avoid using shared-weight convolutional feature extractors. In particular, we have leveraged position and range encodings to design a RAAConv layer with two independent convolution branches, which separately focus on sparse and dense feature extraction. Moreover, the auxiliary density level estimation module (ADLE) has been proposed to further help RAANet extract occlusion information of objects during training. Since RAAConv sets the channel number for each branch to the half of final output channels, and ADLE is not attached during inference, the proposed RAANet is able to run in real-time. Evaluations on nuScenes dataset have shown that our proposed RAANet outperforms the SOTA works. The code is available at the following anonymous link: <https://github.com/anonymous0522/RAAN>.

References

1. Anonymized: Anonymized github repository for our code. <https://github.com/anonymous0522/RAAN> 3, 10
2. Bhattacharyya, P., Huang, C., Czarnecki, K.: Sa-det3d: Self-attention based context-aware 3d object detection. arXiv preprint arXiv:2101.02672 (2021) 9
3. Caesar, H., Bankiti, V., Lang, A.H., Vora, S., Liong, V.E., Xu, Q., Krishnan, A., Pan, Y., Baldan, G., Beijbom, O.: nuscenes: A multimodal dataset for autonomous driving. arXiv preprint arXiv:1903.11027 (2019) 9
4. Chen, Q., Sun, L., Cheung, E., Yuille, A.L.: Every view counts: Cross-view consistency in 3d object detection with hybrid-cylindrical-spherical voxelization. Advances in Neural Information Processing Systems (2020) 9
5. Chen, Q., Sun, L., Wang, Z., Jia, K., Yuille, A.: Object as hotspots: An anchor-free 3d object detection approach via firing of hotspots. In: European Conference on Computer Vision. pp. 68–84. Springer (2020) 9
6. Chen, Q., Vora, S., Beijbom, O.: Polarstream: Streaming lidar object detection and segmentation with polar pillars. arXiv preprint arXiv:2106.07545 (2021) 9
7. Chen, X., Wang, J., Held, D., Hebert, M.: Panonet3d: Combining semantic and geometric understanding for lidar point cloud detection. In: 2020 International Conference on 3D Vision (3DV). pp. 753–761. IEEE (2020) 9
8. Contributors, M.: MMDetection3D: OpenMMLab next-generation platform for general 3D object detection. <https://github.com/open-mmlab/mmdetection3d> (2020) 9
9. Kingma, D.P., Ba, J.: Adam: A method for stochastic optimization. arXiv preprint arXiv:1412.6980 (2014) 10
10. Lang, A.H., Vora, S., Caesar, H., Zhou, L., Yang, J., Beijbom, O.: Pointpillars: Fast encoders for object detection from point clouds. In: Proceedings of the IEEE/CVF Conference on Computer Vision and Pattern Recognition. pp. 12697–12705 (2019) 1, 3, 9, 12
11. Lin, T.Y., Goyal, P., Girshick, R., He, K., Dollár, P.: Focal loss for dense object detection. In: Proceedings of the IEEE international conference on computer vision. pp. 2980–2988 (2017) 5
12. NuScenes: Nuscenes 2d object detection benchmark. <https://www.nuscenes.org/object-detection?externalData=no&mapData=no&modalities=Lidar> 8
13. Paszke, A., Gross, S., Chintala, S., Chanan, G., Yang, E., DeVito, Z., Lin, Z., Desmaison, A., Antiga, L., Lerer, A.: Automatic differentiation in pytorch (2017) 9
14. Rapoport-Lavie, M., Raviv, D.: It’s all around you: Range-guided cylindrical network for 3d object detection. In: Proceedings of the IEEE/CVF International Conference on Computer Vision. pp. 2992–3001 (2021) 9
15. Shi, S., Wang, Z., Shi, J., Wang, X., Li, H.: From points to parts: 3d object detection from point cloud with part-aware and part-aggregation network. IEEE Transactions on Pattern Analysis and Machine Intelligence (2020) 9
16. Smith, L.N., Topin, N.: Super-convergence: Very fast training of neural networks using large learning rates. In: Artificial Intelligence and Machine Learning for Multi-Domain Operations Applications. vol. 11006, p. 1100612. International Society for Optics and Photonics (2019) 10
17. Sun, P., Wang, W., Chai, Y., Elsayed, G., Bewley, A., Zhang, X., Sminchisescu, C., Anguelov, D.: Rsn: Range sparse net for efficient, accurate lidar 3d object detection. In: Proceedings of the IEEE/CVF Conference on Computer Vision and Pattern Recognition. pp. 5725–5734 (2021) 8

18. Wang, J., Lan, S., Gao, M., Davis, L.S.: Infofocus: 3d object detection for autonomous driving with dynamic information modeling. In: European Conference on Computer Vision. pp. 405–420. Springer (2020) [9](#)
19. Woo, S., Park, J., Lee, J.Y., Kweon, I.S.: Cbam: Convolutional block attention module. In: Proceedings of the European conference on computer vision (ECCV). pp. 3–19 (2018) [4](#)
20. Xiong, P., Hao, X., Shao, Y., Yu, J.: Adaptive attention model for lidar instance segmentation. In: Advances in Visual Computing. pp. 141–155. Springer International Publishing (2019) [1](#)
21. Xu, R., Guo, Y., Han, X., Xia, X., Xiang, H., Ma, J.: Opennda: an open cooperative driving automation framework integrated with co-simulation. In: 2021 IEEE International Intelligent Transportation Systems Conference (ITSC). pp. 1155–1162. IEEE (2021) [1](#)
22. Yan, Y., Mao, Y., Li, B.: Second: Sparsely embedded convolutional detection. *Sensors* **18**(10), 3337 (2018) [3](#)
23. Yang, B., Luo, W., Urtasun, R.: Pixor: Real-time 3d object detection from point clouds. In: Proceedings of the IEEE conference on Computer Vision and Pattern Recognition. pp. 7652–7660 (2018) [3](#)
24. Ye, Y., Chen, H., Zhang, C., Hao, X., Zhang, Z.: Sarpnet: Shape attention regional proposal network for lidar-based 3d object detection. *Neurocomputing* **379**, 53–63 (2020). <https://doi.org/https://doi.org/10.1016/j.neucom.2019.09.086>, <https://www.sciencedirect.com/science/article/pii/S0925231219313827> [9](#)
25. Yin, T., Zhou, X., Krähenbühl, P.: Center-based 3d object detection and tracking. *CVPR* (2021) [4](#), [5](#), [9](#)
26. Zhang, H., Goodfellow, I., Metaxas, D., Odena, A.: Self-attention generative adversarial networks. In: International conference on machine learning. pp. 7354–7363. PMLR (2019) [6](#)
27. Zhou, X., Wang, D., Krähenbühl, P.: Objects as points. In: arXiv preprint arXiv:1904.07850 (2019) [5](#)
28. Zhou, Y., Sun, P., Zhang, Y., Anguelov, D., Gao, J., Ouyang, T., Guo, J., Ngiam, J., Vasudevan, V.: End-to-end multi-view fusion for 3d object detection in lidar point clouds. In: Conference on Robot Learning. pp. 923–932. PMLR (2020) [1](#)
29. Zhou, Y., Tuzel, O.: Voxelnet: End-to-end learning for point cloud based 3d object detection. In: Proceedings of the IEEE conference on computer vision and pattern recognition. pp. 4490–4499 (2018) [1](#), [3](#), [5](#)
30. Zhu, B., Jiang, Z., Zhou, X., Li, Z., Yu, G.: Class-balanced grouping and sampling for point cloud 3d object detection. arXiv preprint arXiv:1908.09492 (2019) [9](#)
31. Zhu, X., Ma, Y., Wang, T., Xu, Y., Shi, J., Lin, D.: Ssn: Shape signature networks for multi-class object detection from point clouds. In: Computer Vision—ECCV 2020: 16th European Conference, Glasgow, UK, August 23–28, 2020, Proceedings, Part XXV 16. pp. 581–597. Springer (2020) [9](#)